Cellulose (2023) 30:6773–6785
https://doi.org/10.1007/s10570-023-05254-0

ORIGINAL RESEARCH

$Ti_3C_2T_x$ MXene-incorporated macroporous bacterial cellulose scaffolds with physical and chemical crosslinking for enhanced mechanical and biological performance

Zhiwei Yang · Yichuan Zhang · Yuqin Chen · Zhengzhao Yang · Teng Cui · Honglin Luo · Yue Liu · Yizao Wan

Received: 4 November 2022 / Accepted: 8 May 2023 / Published online: 12 June 2023

Abstract Macroporous bacterial cellulose (MBC) scaffolds composed of BC fragments have received much attention in bone tissue engineering due to their simplicity in preparation process. However, the use of BC fragments and the sole polysaccharide component of BC inevitably lead to MBC scaffolds with low mechanical properties and inadequate biocompatibility and osteogenic property. Herein, physically and chemically crosslinked macroporous BC/$Ti_3C_2T_x$ (pc-MBC/$Ti_3C_2T_x$) scaffolds were successfully prepared by combining physical and chemical crosslinking strategies. The simultaneous physical crosslinking (hydrogen bonds between $Ti_3C_2T_x$ nanosheets and the nanofibers of BC fragments) and chemical crosslinking (amide bonds among the residual trace proteins on the nanofibers of BC fragments) exhibit an obvious synergistic effect on the improvement of mechanical properties of pc-MBC/$Ti_3C_2T_x$ scaffolds. The maximum compressive strength (124.28 ± 5.04 kPa at 80% strain) and modulus (40.78 ± 3.01 kPa) of pc-MBC/$Ti_3C_2T_x$ scaffold are about 3–9 and 3–10 times as high as the counterparts, respectively. In addition, the interconnected macropores can effectively support the migration and penetration of MC3T3-E1 cells into pc-MBC/$Ti_3C_2T_x$ scaffolds. More importantly, pc-MBC/$Ti_3C_2T_x$ scaffolds are superior to the counterpart without $Ti_3C_2T_x$ nanosheets in terms of viability, adhesion, spreading, and osteogenic differentiation of MC3T3-E1 cells. These obtained results indicate that pc-MBC/$Ti_3C_2T_x$ scaffolds hold considerable potential for bone tissue engineering.

Keywords Bacterial cellulose · $Ti_3C_2T_x$ MXene · Macropore · Mechanical property · Biological performance

Zhiwei Yang and Yichuan Zhang have contributed equally to this work.

Supplementary Information The online version contains supplementary material available at https://doi.org/10.1007/s10570-023-05254-0.

Z. Yang · Y. Zhang · Y. Chen · Z. Yang · T. Cui · H. Luo · Y. Wan
Jiangxi Key Laboratory of Nanobiomaterials, School of Materials Science and Engineering, East China Jiaotong University, Nanchang 330013, China

H. Luo · Y. Wan (✉)
School of Materials Science and Engineering, Tianjin University, Tianjin 300072, China
e-mail: yzwan@tju.edu.cn

Y. Liu (✉)
School of Materials Science and Engineering, Linyi University, Linyi 276000, China
e-mail: lyliuyue1990@126.com

Introduction

Bone repair, which is caused by diseases, trauma, aging, etc., is still challenging at present (Qu et al. 2019; Torgbo and Sukyai 2018). Considering the limitations of autografts and allografts in clinical

applications, it is crucial to seek alternative scaffold materials for bone tissue engineering. As a natural polysaccharide polymer, bacterial cellulose (BC) displays unique structure and properties, such as three dimensional (3D) nanofibrous network structure similar to native extracellular matrix (ECM), excellent mechanical properties, and large water-holding capacity (Chen et al. 2022; Liu et al. 2022; Torgbo and Sukyai 2018). These features endow BC with prominent advantages as a potential scaffold material for bone tissue engineering (Torgbo and Sukyai 2018; Zaborowska et al. 2010; Zhang et al. 2020). However, it is commonly documented that the intrinsic small pore sizes (~0.02–10 μm) of BC fail to support cell ingrowth (Gross and Rodríguez-Lorenzo 2004; Wu et al. 2019; Yin et al. 2015). Another limitation is that the biocompatibility and osteogenic property of BC are not as high as desired level because it is only composed of polysaccharide molecules (Wu et al. 2019; Xiao et al. 2022; Xiong et al. 2015). These above-mentioned unfavorable factors limit the applications of BC in bone tissue engineering.

At present, freeze drying method has been widely employed to construct macroporous BC (MBC) scaffolds due to their simplicity in preparation process. It was reported that the macroporous BC-based scaffolds prepared by this strategy held great potential for bone tissue engineering (Noh et al. 2019). Nevertheless, improving the mechanical properties of MBC scaffolds is necessary because the use of BC fragments inevitably leads to poor mechanical properties. Recently, our group creatively introduced chemical crosslinking into MBC scaffolds to endow the chemically crosslinked MBC (c-MBC) scaffolds with enhanced mechanical properties, in which the chemical crosslinking could be attributed to 1-ethyl-3-(3-dimethylaminopropyl) carbodiimide/N-hydroxysuccinimide (EDC/NHS)-induced amide interaction among the protein residues on the nanofibers of BC fragments (Xun et al. 2021). However, the improvement of mechanical properties is still relatively limited due to the small quantity of reaction sites. On the other hand, the biological properties cannot be essentially improved because c-MBC scaffolds have the same polysaccharide component as pristine BC, although the macropores can provide large space to promote cell proliferation and penetration to a certain degree. Therefore, it is highly desirable to further improve the mechanical and biological performance of c-MBC scaffolds for potential applications in bone tissue engineering.

As a new class of two dimensional (2D) nanomaterials, MXenes with a general chemical formula of $M_{n+1}X_nT_x$ (M belongs to an early transition metal; X is carbon and/or nitrogen; and T_x represents surface functional groups, i.e., –OH and –F) have attracted substantial interest because of their good hydrophilicity and solubility, large specific surface area, and high mechanical properties (Huang et al. 2020; Iravani and Varma 2021; Lin et al. 2018, 2021). $Ti_3C_2T_x$ MXene, which is usually prepared by selectively etching Al element of Ti_3AlC_2 MAX phase, is the first candidate among these MXenes (Iravani and Varma 2021; Lin et al. 2018). It has been well documented that MXenes can be employed to enhance the mechanical properties of polymers through physical crosslinking, namely, hydrogen bonds between the surface functional groups of MXenes and the surface functional groups (such as –OH and –C=O) of polymers (Lu et al. 2021; Mao et al. 2020; Zhan et al. 2019). In the previous work, the simultaneous physical and chemical crosslinking exhibited an obvious synergistic effect on endowing hybrid hydrogels with excellent mechanical properties (Xu et al. 2018). Therefore, it is reasonably hypothesized that the simultaneous physical and chemical crosslinking is beneficial to improve the mechanical properties after the incorporation of MXene nanosheets into c-MBC scaffolds. More importantly, it has been reported that the positive role of MXenes in improving the biological properties of scaffold materials for bone tissue engineering due to their outstanding biocompatibility and osteogenic differentiation performance (Chen et al. 2017, 2018; Huang et al. 2020; Iravani and Varma 2021; Lin et al. 2021; Mi et al. 2022). For example, $Ti_3C_2T_x$ MXene composite fibers that were fabricated by electrospinning technique displayed excellent biocompatibility and promoted the differentiation of bone marrow-derived mesenchymal stem cells to osteoblasts compared with the pure polymer counterparts (Huang et al. 2020). Similarly, Kim's group reported that the introduced $Ti_3C_2T_x$ nanosheets were conducive to the adhesion, proliferation, and osteogenic differentiation of MC3T3-E1 cells on poly(lactic acid) membrane (Chen et al. 2018). Moreover, this group claimed that the strong cell affinity of MXenes was confirmed by the theory results based on the first-principles calculations (Chen et al. 2017). Evidently, it may be also

feasible to enhance the biocompatibility and osteogenic performance of c-MBC scaffold by incorporating with MXene nanosheets.

To testify the hypothesis, we introduced $Ti_3C_2T_x$ nanosheets into c-MBC scaffolds to form physically and chemically crosslinked macroporous scaffolds (pc-MBC/$Ti_3C_2T_x$ scaffolds). The effects of the simultaneous physical and chemical crosslinking on the mechanical properties of pc-MBC/$Ti_3C_2T_x$ scaffolds were investigated. Furthermore, the biological experiments were conducted to evaluate whether pc-MBC/$Ti_3C_2T_x$ scaffolds could effectively support the migration and penetration of MC3T3-E1 cells, display excellent biocompatibility, and promote the osteogenic differentiation of MC3T3-E1 cells.

Materials and methods

Preparation of $Ti_3C_2T_x$ nanosheets

In a typical synthesis procedure, 1.2 g of LiF was mixed with 25 mL of 9 M HCl solution in a Teflon vessel under stirring. Then 0.5 g of Ti_3AlC_2 powders (Jilin 11 Technology Co., Ltd., China) was slowly added to the mixed solution and the reaction lasted for 24 h under stirring at 35 °C to remove Al element. Subsequently, the resultant precipitates were repeatedly washed with deionized (DI) water and centrifuged (10 min at 3500 rpm for per cycle) until the pH of the supernatant was not less than 6. Afterwards, the resultant precipitates were sonicated with 50 mL of DI water for 1 h and followed by centrifugation at 3500 rpm for 1 h, yielding uniform $Ti_3C_2T_x$ dispersion. Finally, $Ti_3C_2T_x$ dispersion was frozen at −20 °C for 12 h and freeze dried at −50 °C for 48 h to obtain black $Ti_3C_2T_x$ nanosheets.

Preparation of BC fragments

The white BC aerogels were obtained by the typical static culture according to our previous report (Xun et al. 2021). 500 mg of BC aerogels was mixed with DI water until the total volume reached 100 mL. After the strong mechanical shearing with a high-speed homogenizer (FJ200-SH, Shanghai Shuaijia Electronic Technology Co., Ltd., China) at 12,000 rpm for 60 min, BC aerogels were cut into small fragments, yielding uniform BC dispersion (5 mg/mL).

Preparation of pc-MBC/$Ti_3C_2T_x$ scaffolds

20 mL of BC dispersion was mixed with $Ti_3C_2T_x$ nanosheets under sonication for 1 h. Subsequently, the uniformly mixed dispersion was transferred into 48-well plates (serving as molds), frozen at −20 °C for 12 h, and freeze dried at −50 °C for 48 h to form physically crosslinked macroporous scaffolds (p-MBC/$Ti_3C_2T_x$ scaffolds). Then the chemical crosslinking reaction was allowed to last for 12 h at 30 °C in the dark after immersing p-MBC/$Ti_3C_2T_x$ scaffolds into ethanol absolute containing EDC (5 mg/mL) and NHS (3 mg/mL). After the chemical crosslinking reaction was completed, the obtained pc-MBC/$Ti_3C_2T_x$ scaffolds were washed with DI water for several times, frozen at −20 °C for 12 h, and finally freeze dried at −50 °C for 48 h. For simplify, pc-MBC/$Ti_3C_2T_x$ scaffolds with 1, 5, 10, and 15 wt% $Ti_3C_2T_x$ were denoted as pc-MBC/$Ti_3C_2T_x$-1, pc-MBC/$Ti_3C_2T_x$-2, pc-MBC/$Ti_3C_2T_x$-3, and pc-MBC/$Ti_3C_2T_x$-4, respectively. Similarly, p-MBC/$Ti_3C_2T_x$ scaffold with 10 wt% $Ti_3C_2T_x$ was denoted as p-MBC/$Ti_3C_2T_x$-3; the scaffold without chemical crosslinking or $Ti_3C_2T_x$ nanosheets was denoted as MBC; the chemically crosslinked scaffold without $Ti_3C_2T_x$ nanosheets was denoted as c-MBC.

The whole preparation process of pc-MBC/$Ti_3C_2T_x$ scaffolds is schematically illustrated in Fig. 1. In brief, $Ti_3C_2T_x$ nanosheets were prepared by selectively etching Al layer of Ti_3AlC_2 MAX phase and BC fragments were prepared through mechanically shearing BC aerogels. Then the prepared $Ti_3C_2T_x$ nanosheets and BC fragments were uniformly mixed and freeze dried to form physically crosslinked scaffolds with abundant interconnected macropores. The physical crosslinking can be attributed to the hydrogen bonds between the surface functional groups on $Ti_3C_2T_x$ nanosheets and –OH groups on the nanofibers of BC fragments. Subsequently, the amide reaction is allowed to occur among the trace protein residues on the nanofibers of BC fragments with the assist of EDC/NHS to form chemical crosslinking, finally obtaining pc-MBC/$Ti_3C_2T_x$ scaffolds.

Characterizations

The morphology of pristine $Ti_3C_2T_x$ was characterized by a transmission electron microscope (TEM, JEM-2010 F, JEOL, Japan). The morphologies of the scaffolds were observed by a digital camera (DS126431,

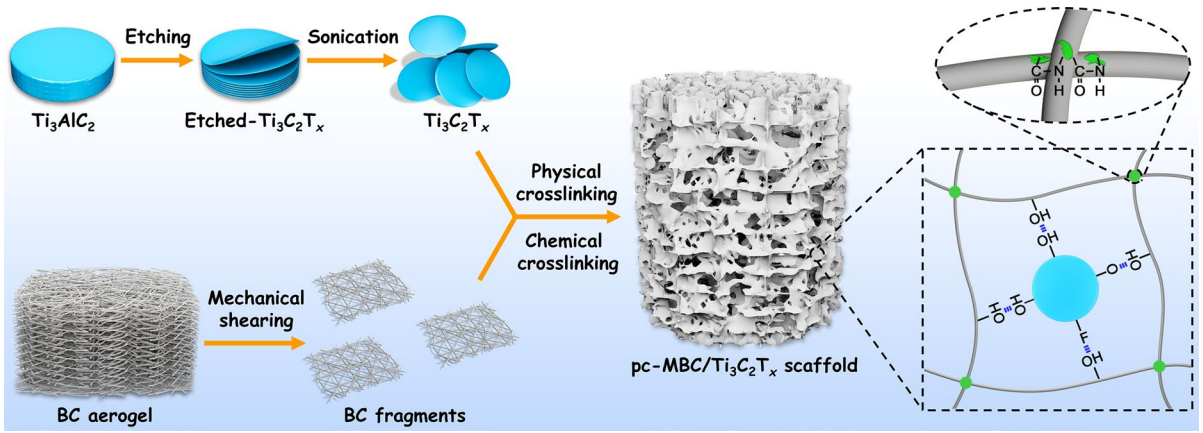

Fig. 1 Schematic illustration of the whole preparation process of pc-MBC/$Ti_3C_2T_x$ scaffolds

Canon, Japan) and a scanning electron microscope (SEM, SU8010, Hitachi, Japan). The pore sizes were measured by an image analysis software (Nano Measurer Version 1.2, China) based on the obtained SEM images (Ou et al. 2016; Xun et al. 2021). The porosities of the scaffolds were evaluated by ethanol immersion method as previously reported (Wu et al. 2021). The measured dry weight and volume of the scaffolds were recorded as W_0 and V_0, respectively. After the scaffolds were immersed in ethanol overnight and taken out, the weight of the ethanol-immersed scaffolds was recorded as W. The porosities were calculated according to the equation of Porosity $= (W - W_0)/\rho V_0 \times 100\%$, where ρ represented the density of ethanol. X-ray diffraction (XRD) patterns were collected on a XRD Diffractometer (XRD-6100, Shimadzu, Japan) with Cu Kα radiation ($\lambda = 0.154$ nm) at a scanning speed of 4° min^{-1}. Fourier transform infrared spectroscopy (FT-IR, Spectrum one, PerkinElmer, USA) was conducted to determine the chemical structure of the scaffolds with a resolution of 4 cm^{-1}. The compressive test was conducted on the scaffolds (~8 mm in diameter and ~10 mm in height) at dry state by an electromagnetic fatigue testing machine (MUF-1050, Tianjin Care Measurement & Control Co., Ltd., China) at a compressive strain rate of 5 mm min^{-1}.

Biological evaluation

MC3T3-E1 cells, which were provided by Procell Life Science & Technology Co., Ltd., China, were used to evaluate the biological properties. The received MC3T3-E1 cells were cultured in Dulbecco's modified Eagle's medium containing 10% fetal bovine serum and 1% penicillin-streptomycin in a 5% CO_2 incubator at 37 °C. The culture medium was refreshed every 2 days. The cultured MC3T3-E1 cells at 80–90% confluence were trypsinized with 0.25% trypsin-EDTA, resuspended in culture medium, and counted by a hemocytometer. After sterilized by ultraviolet irradiation for 30 min, the scaffolds were transferred into 24-well plates. Then MC3T3-E1 cells were seeded onto the scaffolds and cultured in a 5% CO_2 incubator at 37 °C for varying durations. The culture medium was refreshed every 2 days.

Live/dead staining assay was conducted to evaluate cell viability at a seeding density of 3×10^4 cells per well. The cell-seeded scaffolds after cultured for 1, 4, and 7 days were washed with phosphate buffer solution (PBS) for 3 times and then stained with fluorescein diacetate (FDA) and propidium iodide (PI), in which live cells were stained green by FDA and dead cells were stained red by PI. After incubated for 5 min, the stained cells were observed by a confocal laser scanning microscopy (CLSM, TCS SP8, Leica, Germany). The cell viability was further quantitatively evaluated by CCK-8 assay at a seeding density of 3×10^4 cells per well. After cultured for 1, 4, and 7 days, the culture medium was gently removed and the cell-seeded scaffolds were incubated with fresh culture medium containing 10% CCK-8 in the dark for 2 h. Then the culture medium from each well was transferred to a new 96-well plate, respectively. Subsequently, the optical densities were measured

at 450 nm by a microplate reader (iMark, Bio Rad, USA). The cytoskeletons and cell nuclei were strained to evaluate cell adhesion and spreading at a seeding density of 1.5×10^4 cells per well. The cell-seeded scaffolds cultured after 7 days were washed with PBS for 3 times and fixed with 4% paraformaldehyde at room temperature. Then the cells were permeabilized with 0.1% Triton X-100 in PBS for 10 min. After washed with PBS for 3 times, the cytoskeletons were stained red with rhodamine-phalloidin for 30 min. After washed with PBS for 3 times again, the cell nuclei were stained blue with 4′, 6-diamidino-2-phenylindole (DAPI) for 10 min. Finally, the stained cells were visualized by CLSM to observe cell adhesion and spreading. In addition, MC3T3-E1 cells were seeded onto the scaffolds at a density of 3×10^4 cells per well. The cell-seeded scaffolds after 7 days of culture were also treated with the procedures of live staining assay and then the cell spatial distributions were assessed by CLSM in 3D model.

Alkaline phosphatase (ALP) activity of MC3T3-E1 cells cultured with the scaffolds at a seeding density of 3×10^4 cells per well was detected by commercial ALP assay kit to evaluate osteogenic differentiation property. After 7 and 14 days of culture, the culture medium was gently removed and the cell-seeded scaffolds were washed with PBS for 3 times. Then MC3T3-E1 cells were lysed with RIPA lysis buffer. After the lysates were centrifuged at 12,000 rpm for 5 min, the clear supernatant was collected for the assay of ALP activity according to the manufacturer's instructions.

Statistical analysis

SPSS Statistics software (Version 20, SPSS Inc., USA) was employed to perform statistical analysis. The data were expressed as mean value ± standard deviation. The statistical significance was accepted under the condition of $p<0.05$.

Results and discussion

Morphologies and pores of pc-MBC/$Ti_3C_2T_x$ scaffolds

It can be seen from Fig. S1 that $Ti_3C_2T_x$ possesses typical 2D nanosheet feature, which indicates the high quality of $Ti_3C_2T_x$, in line with our previous report (Wan et al. 2021). As expected, the digital photos (Fig. 2a) show that pc-MBC/$Ti_3C_2T_x$ scaffolds gradually darken with the increase of $Ti_3C_2T_x$ content while c-MBC scaffold is white. The low-magnification SEM image in Fig. 2b reveals that a typical c-MBC scaffold contains sheet-like walls and interconnected macropores. Furthermore, the closely intertwined BC fragments are clearly observed in the sheet-like walls at a higher magnification (Fig. 2c). These results of c-MBC scaffold are consistent with our previous report (Xun et al. 2021). After incorporating with $Ti_3C_2T_x$ nanosheets, the obtained pc-MBC/$Ti_3C_2T_x$ scaffolds still exhibit similar morphological and macroporous features to c-MBC scaffold; however, the sheet-like walls and macropore sizes become compact and small with the increase of $Ti_3C_2T_x$ content, respectively (Fig. 2d-k). The morphological changes of sheet-like walls is related with the restacking and aggregation of $Ti_3C_2T_x$ nanosheets at high $Ti_3C_2T_x$ content, which is the common feature of MXenes (Li et al. 2022a; Zhang et al. 2023). In detail, the statistical data based on the SEM images further indicate that the macropore sizes gradually decease from 204.06 ± 3.24 μm of c-MBC scaffold to 144.08 ± 2.17 μm of pc-MBC/$Ti_3C_2T_x$-4 scaffold (Fig. 3a–e). The interconnected macroporous structure is indispensable for scaffolds to allow cell ingrowth. It is commonly accepted that the pore sizes should be larger than 100 μm for bone tissue engineering (Gross and Rodríguez-Lorenzo 2004; Haugen et al. 2019). Therefore, the macropores may be appropriate for the migration and penetration of MC3T3-E1 cells into c-MBC and pc-MBC/$Ti_3C_2T_x$ scaffolds. Moreover, as shown in Fig. 3f, the porosities of pc-MBC/$Ti_3C_2T_x$ scaffolds with 10 and 15 wt% $Ti_3C_2T_x$ tend to decrease compared with that of c-MBC scaffold. Nevertheless, the porosities of all scaffolds still maintain at a high level of above 90%.

Crystal and chemical structures of pc-MBC/$Ti_3C_2T_x$ scaffolds

XRD analysis was performed to detect the crystal structures (Fig. 4a). Evidently, three diffraction peaks at about $2\theta=14.4$, 16.8, and 22.7°, which are ascribed to typical cellulose I, are clearly observed in the XRD pattern of c-MBC and pc-MBC/$Ti_3C_2T_x$ scaffolds. According to the previous reports (French 2014; Panaitescu et al. 2016; Singhsa et al. 2018), these three

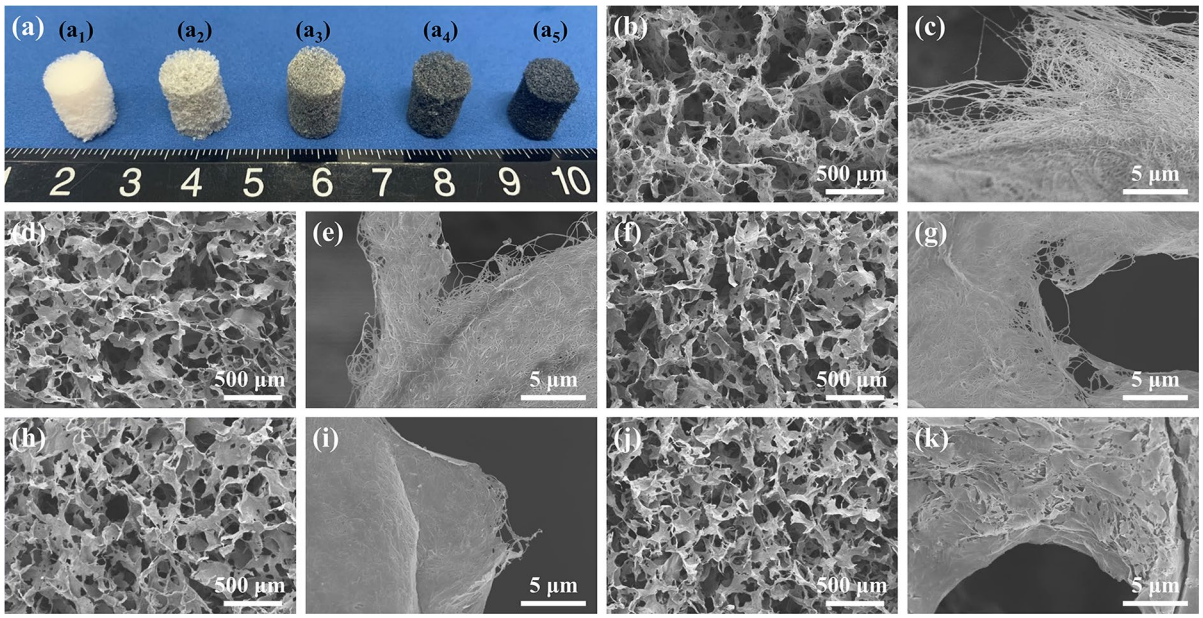

Fig. 2 Digital photos of scaffold samples (**a**): c-MBC (a_1), pc-MBC/$Ti_3C_2T_x$-1 (a_2), pc-MBC/$Ti_3C_2T_x$-2 (a_3), pc-MBC/$Ti_3C_2T_x$-3 (a_4), and pc-MBC/$Ti_3C_2T_x$-4 (a_5); SEM images of scaffold samples: c-MBC (**b** and **c**), pc-MBC/$Ti_3C_2T_x$-1 (**d** and **e**), pc-MBC/$Ti_3C_2T_x$-2 (**f** and **g**), pc-MBC/$Ti_3C_2T_x$-3 (**h** and **i**), and pc-MBC/$Ti_3C_2T_x$-4 (**j** and **k**)

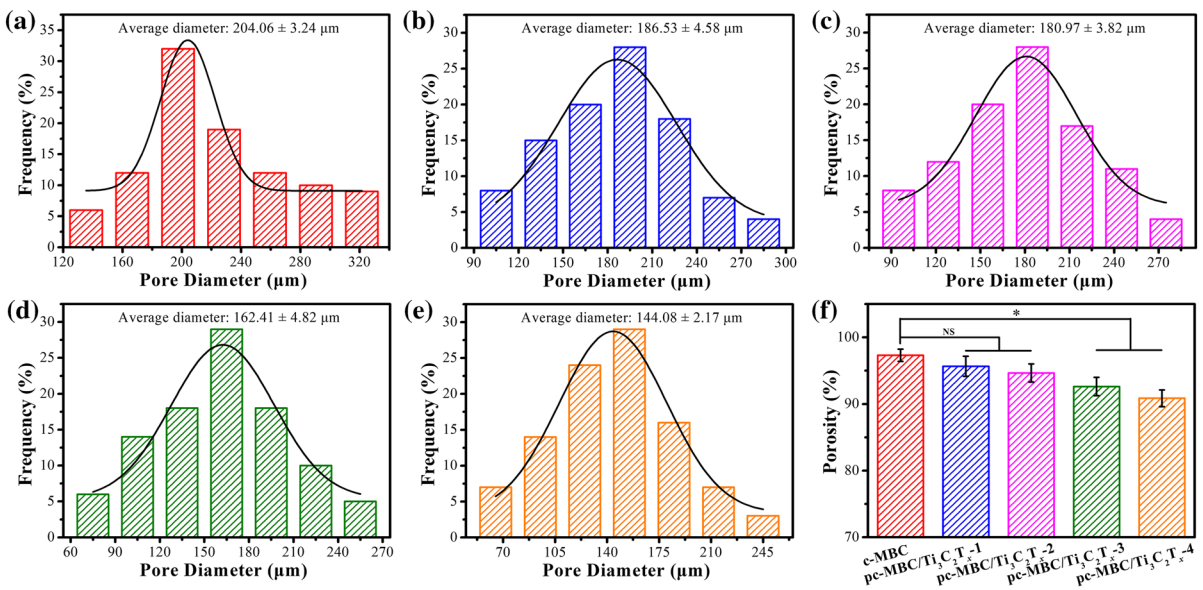

Fig. 3 Pore size distributions of scaffold samples: c-MBC (**a**), pc-MBC/$Ti_3C_2T_x$-1 (**b**), pc-MBC/$Ti_3C_2T_x$-2 (**c**), pc-MBC/$Ti_3C_2T_x$-3 (**d**), and pc-MBC/$Ti_3C_2T_x$-4 (**e**); porosities of c-MBC and pc-MBC/$Ti_3C_2T_x$ scaffolds (**f**), $^*p < 0.05$, $n = 5$

diffraction peaks from low to high degree mainly correspond to (100), (010), and (110) planes of cellulose I_α, respectively. In addition, the characteristic diffraction peak corresponding to (002) plane of $Ti_3C_2T_x$ is also detected in the XRD patterns of pristine $Ti_3C_2T_x$ and pc-MBC/$Ti_3C_2T_x$ scaffolds (Cao et al. 2018; Wan et al.

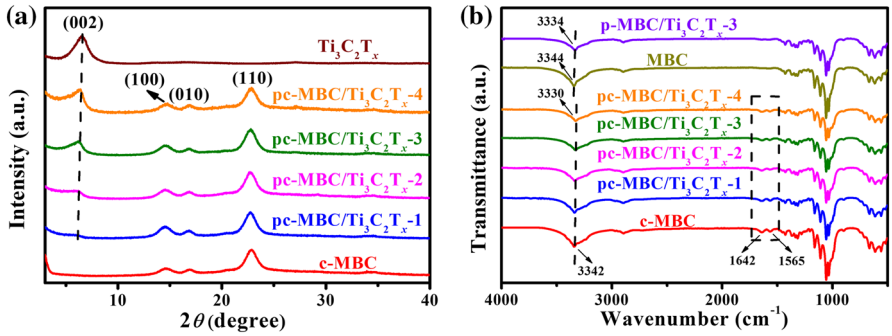

Fig. 4 XRD patterns of pristine $Ti_3C_2T_x$, c-MBC, and pc-MBC/$Ti_3C_2T_x$ scaffolds (**a**); FT-IR spectra of c-MBC, pc-MBC/$Ti_3C_2T_x$, MBC, and p-MBC/$Ti_3C_2T_x$-3 scaffolds (**b**)

2021). It should be mentioned that this diffraction peak gradually shifts from $2\theta = 6.6°$ for pristine $Ti_3C_2T_x$ to $2\theta = 5.8°$ for pc-MBC/$Ti_3C_2T_x$-1 scaffold with the decrease of $Ti_3C_2T_x$ content, in line with the previous reports (Cao et al. 2018; Mao et al. 2020). Correspondingly, the *d*-spacing of $Ti_3C_2T_x$ nanosheets enlarges from 1.34 nm for pristine $Ti_3C_2T_x$ to 1.52 nm for pc-MBC/$Ti_3C_2T_x$-1 scaffold, which confirms the intercalation of nanofibers of BC fragments into $Ti_3C_2T_x$ nanosheets (Jiao et al. 2019). In other words, $Ti_3C_2T_x$ nanosheets tend to restack and aggregate at high $Ti_3C_2T_x$ content, consistent with the SEM results. As shown in Fig. 4b, the FT-IR spectrum of c-MBC scaffold displays a strong band at about 3342 cm^{-1}, which corresponds to the stretching vibration of –OH groups (Luo et al. 2020). However, this band in the FT-IR spectra of pc-MBC/$Ti_3C_2T_x$ scaffolds exhibits an obvious red shift to a certain degree. Moreover, the similar red shift is also observed in the FT-IR spectra of MBC and p-MBC/$Ti_3C_2T_x$ scaffolds. These results indicate the establishment of hydrogen bonds between the surface functional groups on $Ti_3C_2T_x$ nanosheets and –OH groups on the nanofibers of BC fragments (Mao et al. 2020, 2021; Pi et al. 2021; Wang et al. 2021). On the other hand, Fig. 4b also shows that the chemically crosslinked scaffolds (c-MBC and pc-MBC/$Ti_3C_2T_x$) display two extra peaks at about 1642 (amide I) and 1565 (amide II) cm^{-1} compared with the scaffolds without chemical crosslinking (MBC and p-MBC/$Ti_3C_2T_x$-3), which effectively confirms the presence of amide bonds, responsible for the chemical crosslinking in c-MBC and pc-MBC/$Ti_3C_2T_x$ scaffolds. The formation of amide bonds can be attributed to the residual trace proteins on the nanofibers of BC fragments (Xun et al. 2021). The simultaneous physical and chemical crosslinking can effectively contribute to the mechanical properties of pc-MBC/$Ti_3C_2T_x$ scaffolds.

Mechanical properties of pc-MBC/$Ti_3C_2T_x$ scaffolds

As shown in Fig. 5a, the compressive stress-strain curves of all the prepared scaffolds can be divided into three regions (Song et al. 2018). In the first region (compressive strain: < 30%), there exists a distinct linear relation between the compressive stress and strain, representing the elastic deformation stage

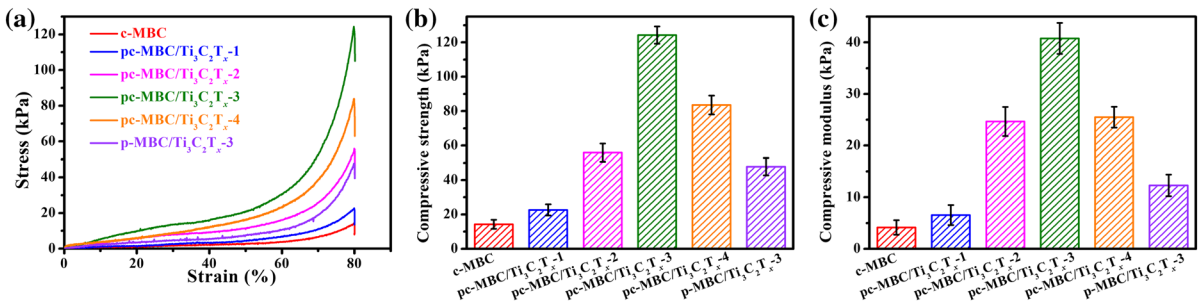

Fig. 5 Compressive properties of c-MBC, pc-MBC/$Ti_3C_2T_x$, and p-MBC/$Ti_3C_2T_x$-3 scaffolds at 80% strain: typical compressive stress-strain curves (**a**), compressive strength (**b**), and compressive modulus (**c**). $n = 5$

of the scaffolds. The stress plateau stage is observed during the second region (compressive strain: 30–50%), in which the compressive stress increases slightly with the compressive strain and the porous structure gradually collapses. In the third region (compressive strain: 50–80%), the compressive strain sharply increases with the compressive strain, which is related with the densification process of the scaffolds under compressure. Notably, as shown in Fig. 5b and c, c-MBC scaffold displays relatively compressive strength and modulus may due to the small quantity of reaction sites. After incorporating with $Ti_3C_2T_x$ nanosheets, the obtained pc-MBC/$Ti_3C_2T_x$ scaffolds display significantly enhanced compressive strength and modulus. In particular, pc-MBC/$Ti_3C_2T_x$-3 scaffold shows the maximum compressive strength (124.28 ± 5.04 kPa at 80% strain) and modulus (40.78 ± 3.01 kPa) among these pc-MBC/$Ti_3C_2T_x$ scaffolds, which are about 9 and 10 times as high as c-MBC scaffold, respectively. Furthermore, both the compressive strength (at 80% strain) and modulus of pc-MBC/$Ti_3C_2T_x$-3 scaffold are about 3 times as high as those of p-MBC/$Ti_3C_2T_x$-3 scaffold, respectively. According to these obtained results, it can be reasonably concluded that the significant improvement of compressive properties can be ascribed to the simultaneous physical and chemical crosslinking in pc-MBC/$Ti_3C_2T_x$ scaffolds. That is to say, there exists a synergetic effect between physical and chemical crosslinking in improving compressive properties (Xu et al. 2018). The compressive strength and modulus of pc-MBC/$Ti_3C_2T_x$-3 scaffold are higher than those of c-MBC scaffold (Li et al. 2022b; Wan et al. 2018), chemically crosslinked BC/cellulose acetate nano/submicrofibrous scaffold (Wan et al. 2018), and chemically crosslinked BC/decellularized ECM scaffold ((Li et al. 2022b), almost equal to those of $Ti_3C_2T_x$-modified collagen/silk/hydroxyapatite scaffold (Li et al. 2021), but still lower than those of silk fibroin/BC/$Ti_3C_2T_x$ scaffold (Ling et al. 2022), respectively. Unfortunately, the excess $Ti_3C_2T_x$ content is unfavorable for compressive strength and modulus of pc-MBC/$Ti_3C_2T_x$ scaffold. The similar results were also reported by the previous works (Mao et al. 2020; Wan et al. 2021). Our previous work revealed that $Ti_3C_2T_x$/BC film with moderate $Ti_3C_2T_x$ content displayed the maximum tensile strength and Young's modulus (Wan et al. 2021). In addition, the excess $Ti_3C_2T_x$ content was not always beneficial to the compressive modulus and Young's modulus of regenerated BC/$Ti_3C_2T_x$ hydrogel (Mao et al. 2020). It has been widely acknowledged that $Ti_3C_2T_x$ nanosheets can significantly enhance the mechanical properties of polymers through physical crosslinking between MXenes and polymers (Lu et al. 2021; Mao et al. 2020; Wan et al. 2021; Zhan et al. 2019). However, the changes of XRD results and the sheet-like walls indicate that $Ti_3C_2T_x$ nanosheets tend to restack and aggregate at high $Ti_3C_2T_x$ content, which adversely affects the mechanical properties (Mao et al. 2020; Zhang et al. 2007). Therefore, the decreased compressive strength and modulus of pc-MBC/$Ti_3C_2T_x$-4 scaffold may mainly results from the restacking and aggregation of $Ti_3C_2T_x$ nanosheets. The relation between $Ti_3C_2T_x$ content and the compressive properties of pc-MBC/$Ti_3C_2T_x$ scaffolds still requires in depth investigation in the future.

Biological properties of pc-MBC/$Ti_3C_2T_x$ scaffolds

Figure 6 show the CLSM images of live/dead stained MC3T3-E1 cells cultured with c-MBC and pc-MBC/$Ti_3C_2T_x$ scaffolds after varying durations. Negligible dead cells are observed for all the scaffolds, indicating that there is no obvious cytotoxicity. After 1 day of culture, the numbers of live cells cultured with c-MBC and pc-MBC/$Ti_3C_2T_x$ scaffolds are similar. With prolonged culture time, more and more live MC3T3-E1 cells with cluster morphology are observed on pc-MBC/$Ti_3C_2T_x$ scaffolds, especially pc-MBC/$Ti_3C_2T_x$-3 scaffold; however, the numbers of live cells cultured with c-MBC scaffold increase very slowly. Furthermore, CCK-8 assay was conducted to quantitatively evaluate cell viability (Fig. 7). After 1 day of culture, there is no significant difference in cell proliferation levels between c-MBC and pc-MBC/$Ti_3C_2T_x$ scaffolds. With prolonged culture time, c-MBC and pc-MBC/$Ti_3C_2T_x$ scaffolds display significantly different cell proliferation trends. MC3T3-E1 cells cultured with pc-MBC/$Ti_3C_2T_x$ scaffolds exhibit significantly higher proliferation levels than those cultured with c-MBC scaffold after 4 and 7 days of culture. Note that pc-MBC/$Ti_3C_2T_x$-3 scaffold displays superior cell proliferation level to the other pc-MBC/$Ti_3C_2T_x$ scaffolds. Furthermore, the cytoskeletons and cell nuclei of MC3T3-E1 cells cultured with the scaffolds after 7 days were strained red and blue, respectively. As shown in Fig. 8 and

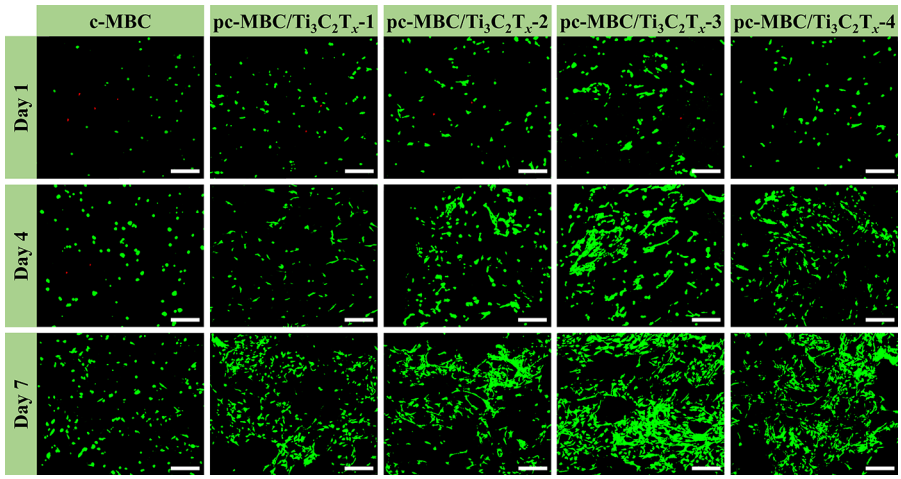

Fig. 6 CLSM images of live/dead stained MC3T3-E1 cells cultured with c-MBC and pc-MBC/$Ti_3C_2T_x$ scaffolds after 1, 4, and 7 days (live cells: green fluorescence; dead cells: red fluorescence). Scale bar: 200 μm

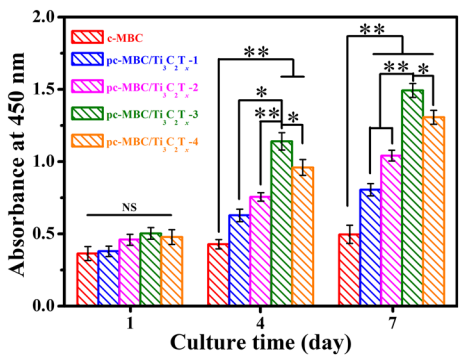

Fig. 7 Proliferation of MC3T3-E1 cells cultured with c-MBC and pc-MBC/$Ti_3C_2T_x$ scaffolds after 1, 4, and 7 days. $*p<0.05$, $**p<0.01$, $n=5$

Fig. S2, MC3T3-E1 cells cultured with pc-MBC/$Ti_3C_2T_x$-3 scaffold displays larger spreading areas with better cytoskeletons than those cultured with c-MBC and the other pc-MBC/$Ti_3C_2T_x$ scaffolds, implying that pc-MBC/$Ti_3C_2T_x$-3 scaffolds can promote the adhesion and spreading of MC3T3-E1 cells well compared with c-MBC and the other pc-MBC/$Ti_3C_2T_x$ scaffolds. On all these counts, the live/dead staining, CCK-8 assay, and rhodamine-phalloidin/DAPI staining results reveal that pc-MBC/$Ti_3C_2T_x$ scaffolds display significantly higher biocompatibility than c-MBC scaffold, especially pc-MBC/$Ti_3C_2T_x$-3 scaffold.

The role of macropores in cell migration and penetration into the scaffolds was estimated by 3D CLSM observation. As shown in Fig. 9, the 3D CLSM images reveal that the macropores allow MC3T3-E1

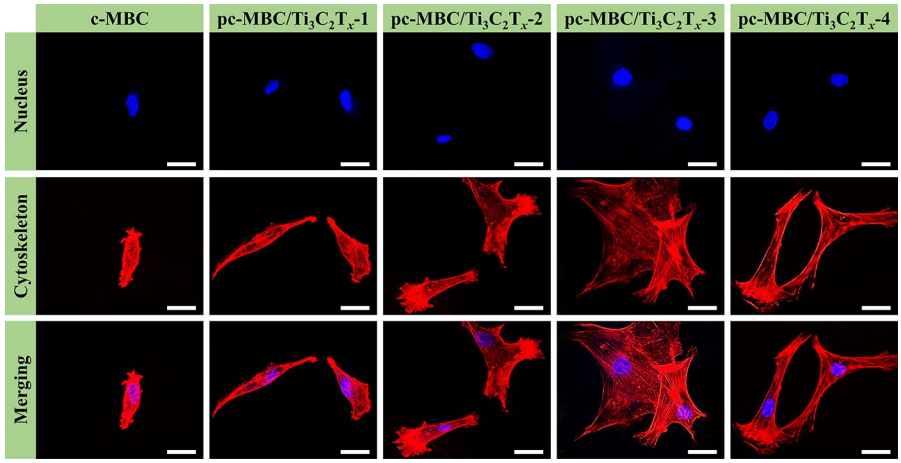

Fig. 8 CLSM images of stained cytoskeletons and cell nuclei of MC3T3-E1 cells cultured with c-MBC and pc-MBC/$Ti_3C_2T_x$ scaffolds after 7 days. Scale bar: 25 μm

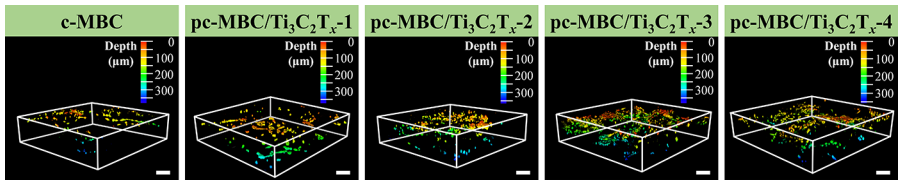

Fig. 9 3D CLSM images of live strained MC3T3-E1 cells cultured with c-MBC and pc-MBC/$Ti_3C_2T_x$ scaffolds after 7 days. Scale bar: 200 μm

cells to migrate and penetrate into c-MBC and pc-MBC/$Ti_3C_2T_x$ scaffolds. Furthermore, the cell penetration distances are similar between c-MBC and pc-MBC/$Ti_3C_2T_x$ scaffolds although the pore sizes of the scaffolds range from 204.06 ± 3.24 μm of c-MBC scaffold to 144.08 ± 2.17 μm of pc-MBC/$Ti_3C_2T_x$-4 scaffold. It is commonly accepted that the pore sizes of the scaffolds should be larger than 100 μm for bone tissue engineering (Gross and Rodríguez-Lorenzo 2004; Haugen et al. 2019). Evidently, all the macropores contained in c-MBC and pc-MBC/$Ti_3C_2T_x$ scaffolds can be capable of supporting the ingrowth of MC3T3-E1 cells. In contrast, the cells only stay on the surface of pristine BC due to the lack of interconnected macropores (Luo et al. 2020; Yin et al. 2015). Therefore, it can be concluded that the biocompatibility differences of these as-prepared scaffolds mainly depend on $Ti_3C_2T_x$ nanosheets instead of pore sizes.

In fact, the positive role of $Ti_3C_2T_x$ nanosheets in promoting biocompatibility in terms of cell viability, adhesion, and spreading has been confirmed by many related reports (Chen et al. 2017, 2018; Huang et al. 2020; Iravani and Varma 2021; Lin et al. 2018, 2021). The improved biocompatibility of pc-MBC/$Ti_3C_2T_x$ scaffold can be attributed to the highly bioactive functional groups of $Ti_3C_2T_x$ nanosheets and excellent biocompatible titanium-based species after the degradation of $Ti_3C_2T_x$ nanosheets (Luo et al. 2019; Mi et al. 2022). Note that pc-MBC/$Ti_3C_2T_x$ scaffold with moderate $Ti_3C_2T_x$ content obtains the best biocompatibility, in line with the previously reported $Ti_3C_2T_x$ MXene composite scaffolds (Mi et al. 2022). Similarly, the related report also revealed that the excess or low graphene oxide was unfavorable for the biocompatibility of silk fibroin scaffold (Wang et al. 2015).

It is commonly acknowledged that ALP activity is an early marker of osteogenic differentiation (Priya et al. 2021; Wan et al. 2022). The quantitative analysis of ALP activities after 7 and 14 days of culture was performed. As shown in Fig. 10, pc-MBC/$Ti_3C_2T_x$ scaffolds show significantly higher ALP

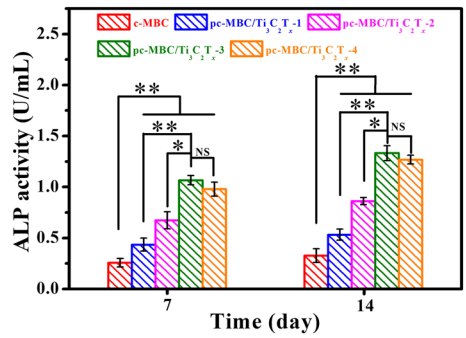

Fig. 10 ALP activity of MC3T3-E1 cells cultured with c-MBC and pc-MBC/$Ti_3C_2T_x$ scaffolds after 7 and 14 days. *$p < 0.05$, **$p < 0.01$, $n = 5$

activities than c-MBC scaffold after 7 and 14 days of culture, indicating the excellent osteogenic performance of pc-MBC/$Ti_3C_2T_x$ scaffolds. This may be also attributed to the presence of titanium-based species after the degradation of $Ti_3C_2T_x$ nanosheets (Mi et al. 2022; Pan et al. 2020). Similar to the biocompatibility, the osteogenic property of pc-MBC/$Ti_3C_2T_x$ scaffolds is not always enhanced with the increase of $Ti_3C_2T_x$ content. This phenomenon is also consistent with the reported result on $Ti_3C_2T_x$ MXene composite scaffolds (Mi et al. 2022).

Conclusions

In this work, physically and chemically crosslinked macroporous scaffolds composed of BC fragments and $Ti_3C_2T_x$ nanosheets have been developed. Compared with c-MBC and p-MBC/$Ti_3C_2T_x$ scaffolds, pc-MBC/$Ti_3C_2T_x$ scaffolds display significantly improved mechanical properties due to the synergistic effect between physical and chemical crosslinking. Moreover, pc-MBC/$Ti_3C_2T_x$ scaffolds are almost equal to c-MBC scaffold in ensuring the migration and penetration of MC3T3-E1 cells. More importantly, pc-MBC/$Ti_3C_2T_x$ scaffolds possess significantly improved biocompatibility and promote osteogenic differentiation

of MC3T3-E1 cells compared with c-MBC scaffold, especially pc-MBC/$Ti_3C_2T_x$ scaffold with 10 wt% $Ti_3C_2T_x$. The proposed hypothesis has been confirmed by the experiment results. Although more efforts should be dedicated to the detailed effect of $Ti_3C_2T_x$ content on the physical/chemical and biological properties in the future work, we believe that the prepared pc-MBC/$Ti_3C_2T_x$ scaffolds hold great potential as scaffold materials for bone tissue engineering due to their enhanced mechanical properties, biocompatibility, and osteogenic performance.

Acknowledgments Not applicable.

Author contributions ZY: Methodology, Writing-original draft, Funding acquisition. YZ: Methodology, Investigation, Validation. YC: Data curation, Funding acquisition. ZY: Conceptualization. TC: Formal analysis. HL: Methodology, Funding acquisition. YL: Conceptualization, Writing-review and editing. YW: Writing-review and editing, Supervision, Project administration.

Funding This work was supported by the National Natural Science Foundation of China (Grant Nos. 32000947 and 31870963), Jiangxi Provincial Natural Science Foundation (Grant Nos. 20202ACBL214007 and 20202ACBL204013), and Jiangxi Provincial Graduate Innovation Special Fund Project (Grant No. YC2022-s569).

Data availability All data generated or analyzed during this work are included in this publication.

Declarations

Conflict of interest The authors declare that there are no known conflicts of interest associated with this publication and there has been no financial support for this work that could have influenced its outcome.

Consent for publication Not applicable.

Ethical approval and consent to participate This article does not contain any studies with human participants or animals performed by any of the authors.

References

Cao W-T, Chen F-F, Zhu Y-J, Zhang Y-G, Jiang Y-Y, Ma M-G, Chen F (2018) Binary strengthening and toughening of MXene/cellulose nanofiber composite paper with nacre-inspired structure and superior electromagnetic interference shielding properties. ACS Nano 12:4583–4593. https://doi.org/10.1021/acsnano.8b00997

Chen K, Qiu N, Deng Q, Kang M-H, Yang H, Baek J-U, Koh Y-H, Du S, Huang Q, Kim H-E (2017) Cytocompatibility of Ti_3AlC_2, Ti_3SiC_2, and Ti_2AlN: in vitro tests and first-principles calculations. ACS Biomater Sci Eng 3:2293–2301. https://doi.org/10.1021/acsbiomaterials.7b00432

Chen K, Chen Y, Deng Q, Jeong S-H, Jang T-S, Du S, Kim H-E, Huang Q, Han C-M (2018) Strong and biocompatible poly(lactic acid) membrane enhanced by $Ti_3C_2T_z$ (MXene) nanosheets for Guided bone regeneration. Mater Lett 229:114–117. https://doi.org/10.1016/j.matlet.2018.06.063

Chen C, Ding W, Zhang H, Zhang L, Huang Y, Fan M, Yang J, Sun D (2022) Bacterial cellulose-based biomaterials: from fabrication to application. Carbohydr Polym 278:118995. https://doi.org/10.1016/j.carbpol.2021.118995

French AD (2014) Idealized powder diffraction patterns for cellulose polymorphs. Cellulose 21:885–896. https://doi.org/10.1007/s10570-013-0030-4

Gross KA, Rodríguez-Lorenzo LM (2004) Biodegradable composite scaffolds with an interconnected spherical network for bone tissue engineering. Biomaterials 25:4955–4962. https://doi.org/10.1016/j.biomaterials.2004.01.046

Haugen HJ, Lyngstadaas SP, Rossi F, Perale G (2019) Bone grafts: which is the ideal biomaterial? J Clin Periodontol 46:92–102. https://doi.org/10.1111/jcpe.13058

Huang R, Chen X, Dong Y, Zhang X, Wei Y, Yang Z, Li W, Guo Y, Liu J, Yang Z, Wang H, Jin L (2020) MXene composite nanofibers for cell culture and tissue engineering. ACS Appl Bio Mater 3:2125–2131. https://doi.org/10.1021/acsabm.0c00007

Iravani S, Varma RS (2021) MXenes and MXene-based materials for tissue engineering and regenerative medicine: recent advances. Mater Adv 2:2906–2917. https://doi.org/10.1039/d1ma00189b

Jiao S, Zhou A, Wu M, Hu H (2019) Kirigami patterning of MXene/bacterial cellulose composite paper for all-solid-state stretchable micro-supercapacitor arrays. Adv Sci 6:1900529. https://doi.org/10.1002/advs.201900529

Li F, Yan Y, Wang Y, Fan Y, Zou H, Liu H, Luo R, Li R, Liu H (2021) A bifunctional MXene-modified scaffold for photothermal therapy and maxillofacial tissue regeneration. Regen Biomater 8:rbab057. https://doi.org/10.1093/rb/rbab057

Li K, Li J, Zhu Q, Xu B (2022a) Three-dimensional MXenes for supercapacitors: a review. Small Methods 6:2101537. https://doi.org/10.1002/smtd.202101537

Li Y, Xun X, Xu Y, Zhan A, Gao E, Yu F, Wang Y, Luo H, Yang C (2022b) Hierarchical porous bacterial cellulose scaffolds with natural biomimetic nanofibrous structure and a cartilage tissue-specific microenvironment for cartilage regeneration and repair. Carbohydr Polym 276:118790. https://doi.org/10.1016/j.carbpol.2021.118790

Lin H, Chen Y, Shi J (2018) Insights into 2D MXenes for versatile biomedical applications: current advances and challenges ahead. Adv Sci 5:1800518. https://doi.org/10.1002/advs.201800518

Lin X, Li Z, Qiu J, Wang Q, Wang J, Zhang H, Chen T (2021) Fascinating MXene nanomaterials: emerging opportunities in the biomedical field. Biomater Sci 9:5437–5471. https://doi.org/10.1039/d1bm00526j

Ling T, Zha X, Zhou K, Zhao X, Jia J, Pan K, Chen A, Yang W, Zhou Z (2022) A facile strategy toward hierarchically

porous composite scaffold for osteosarcoma ablation and massive bone defect repair. Compos Part B 234:109660. https://doi.org/10.1016/j.compositesb.2022.109660

Liu L, Ji X, Mao L, Wang L, Chen K, Shi Z, Ahmed AAQ, Thomas S, Vasilievich RV, Xiao L, Li X, Yang G (2022) Hierarchical-structured bacterial cellulose/potato starch tubes as potential small-diameter vascular grafts. Carbohydr Polym 281:119034. https://doi.org/10.1016/j.carbpol.2021.119034

Lu Z, Jia F, Zhuo L, Ning D, Gao K, Xie F (2021) Microporous MXene/Aramid nanofibers hybrid aerogel with reversible compression and efficient EMI shielding performance. Compos Part B 217:108853. https://doi.org/10.1016/j.compositesb.2021.108853

Luo H, Ao H, Peng M, Yao F, Yang Z, Wan Y (2019) Effect of highly dispersed graphene and graphene oxide in 3D nanofibrous bacterial cellulose scaffold on cell responses: a comparative study. Mater Chem Phys 235:121774. https://doi.org/10.1016/j.matchemphys.2019.121774

Luo H, Gan D, Gama M, Tu J, Yao F, Zhang Q, Ao H, Yang Z, Li J, Wan Y (2020) Interpenetrated nano- and submicro-fibrous biomimetic scaffolds towards enhanced mechanical and biological performances. Mater Sci Eng C 108:110416. https://doi.org/10.1016/j.msec.2019.110416

Mao L, Hu S, Gao Y, Wang L, Zhao W, Fu L, Cheng H, Xia L, Xie S, Ye W, Shi Z, Yang G (2020) Biodegradable and electroactive regenerated bacterial cellulose/MXene ($Ti_3C_2T_x$) composite hydrogel as wound dressing for accelerating skin wound healing under electrical stimulation. Adv Healthc Mater 9:2000872. https://doi.org/10.1002/adhm.202000872

Mao L, Wang L, Zhang M, Ullah MW, Liu L, Zhao W, Li Y, Ahmed AAQ, Cheng H, Shi Z, Yang G (2021) In situ synthesized selenium nanoparticles-decorated bacterial cellulose/gelatin hydrogel with enhanced antibacterial, antioxidant, and anti-inflammatory capabilities for facilitating skin wound healing. Adv Healthc Mater 10:2100402. https://doi.org/10.1002/adhm.202100402

Mi X, Su Z, Fu Y, Li S, Mo A (2022) 3D printing of Ti_3C_2-MXene-incorporated composite scaffolds for accelerated bone regeneration. Biomed Mater 17:035002. https://doi.org/10.1088/1748-605x/ac5ffe

Noh YK, Dos Santos Da Costa A, Park YS, Du P, Kim I-H, Park K (2019) Fabrication of bacterial cellulose-collagen composite scaffolds and their osteogenic effect on human mesenchymal stem cells. Carbohydr Polym 219:210–218. https://doi.org/10.1016/j.carbpol.2019.05.039

Ou R, Wei J, Jiang L, Simon GP, Wang H (2016) Robust thermoresponsive polymer composite membrane with switchable superhydrophilicity and superhydrophobicity for efficient oil-water separation. Environ Sci Technol 50:906–914. https://doi.org/10.1021/acs.est.5b03418

Pan S, Yin J, Yu L, Zhang C, Zhu Y, Gao Y, Chen Y (2020) 2D MXene-integrated 3D-printing scaffolds for augmented osteosarcoma phototherapy and accelerated tissue reconstruction. Adv Sci 7:1901511. https://doi.org/10.1002/advs.201901511

Panaitescu DM, Frone AN, Chiulan I, Casarica A, Nicolae CA, Ghiurea M, Trusca R, Damian CM (2016) Structural and morphological characterization of bacterial cellulose nano-reinforcements prepared by mechanical route. Mater Des 110:790–801. https://doi.org/10.1016/j.matdes.2016.08.052

Pi M, Jiang L, Wang Z, Cui W, Shi L, Ran R (2021) Robust and ultrasensitive hydrogel sensors enhanced by MXene/cellulose nanocrystals. J Mater Sci 56:8871–8886. https://doi.org/10.1007/s10853-020-05644-w

Priya G, Madhan B, Narendrakumar U, Suresh Kumar RV, Manjubala I (2021) In vitro and in vivo evaluation of carboxymethyl cellulose scaffolds for bone tissue engineering applications. ACS Omega 6:1246–1253. https://doi.org/10.1021/acsomega.0c04551

Qu H, Fu H, Han Z, Sun Y (2019) Biomaterials for bone tissue engineering scaffolds: a review. RSC Adv 9:26252–26262. https://doi.org/10.1039/c9ra05214c

Singhsa P, Narain R, Manuspiya H (2018) Physical structure variations of bacterial cellulose produced by different Komagataeibacter xylinus strains and carbon sources in static and agitated conditions. Cellulose 25:1571–1581. https://doi.org/10.1007/s10570-018-1699-1

Song J, Chen C, Yang Z, Kuang Y, Li T, Li Y, Huang H, Kierzewski I, Liu B, He S, Gao T, Yuruker SU, Gong A, Yang B, Hu L (2018) Highly compressible, anisotropic aerogel with aligned cellulose nanofibers. ACS Nano 12:140–147. https://doi.org/10.1021/acsnano.7b04246

Torgbo S, Sukyai P (2018) Bacterial cellulose-based scaffold materials for bone tissue engineering. Appl Mater Today 11:34–49. https://doi.org/10.1016/j.apmt.2018.01.004

Wan Y, Cui T, Zhang Q, Yang Z, Yao F, Luo H (2018) Submicrofiber-incorporated 3D bacterial cellulose nanofibrous scaffolds with enhanced cell performance. Macromol Mater Eng 303:1800316. https://doi.org/10.1002/mame.201800316

Wan Y, Xiong P, Liu J, Feng F, Xun X, Gama FM, Zhang Q, Yao F, Yang Z, Luo H, Xu Y (2021) Ultrathin, strong, and highly flexible $Ti_3C_2T_x$ MXene/bacterial cellulose composite films for high-performance electromagnetic interference shielding. ACS Nano 15:8439–8449. https://doi.org/10.1021/acsnano.0c10666

Wan H-Y, Shin RLY, Chen JCH, Assunção M, Wang D, Nilsson SK, Tuan RS, Blocki A (2022) Dextran sulfate-amplified extracellular matrix deposition promotes osteogenic differentiation of mesenchymal stem cells. Acta Biomater 140:163–177. https://doi.org/10.1016/j.actbio.2021.11.049

Wang L, Lu C, Li Y, Wu F, Zhao B, Dong X (2015) Green fabrication of porous silk fibroin/graphene oxide hybrid scaffolds for bone tissue engineering. RSC Adv 5:78660–78668. https://doi.org/10.1039/c5ra12173f

Wang Z, Han X, Han X, Chen Z, Wang S, Pu J (2021) MXene/wood-derived hierarchical cellulose scaffold composite with superior electromagnetic shielding. Carbohydr Polym 254:117033. https://doi.org/10.1016/j.carbpol.2020.117033

Wu J, Yin N, Chen S, Weibel DB, Wang H (2019) Simultaneous 3D cell distribution and bioactivity enhancement of bacterial cellulose (BC) scaffold for articular cartilage tissue engineering. Cellulose 26:2513–2528. https://doi.org/10.1007/s10570-018-02240-9

Wu M, Chen F, Wu P, Yang Z, Zhang S, Xiao L, Deng Z, Zhang C, Chen Y, Cai L (2021) Nanoclay mineral-reinforced macroporous nanocomposite scaffolds for in situ

bone regeneration: in vitro and in vivo studies. Mater Des 205:109734. https://doi.org/10.1016/j.matdes.2021.109734

Xiao J, Wei Q, Xue J, Liu Z, Li Z, Zhou Z, Chen F, Zhao F (2022) Mesoporous bioactive glass/bacterial cellulose composite scaffolds for bone support materials. Colloids Surf A 642:128693. https://doi.org/10.1016/j.colsurfa.2022.128693

Xiong G, Luo H, Zhang C, Zhu Y, Wan Y (2015) Enhanced biological behavior of bacterial cellulose scaffold by creation of macropores and surface immobilization of collagen. Macromol Res 23:734–740. https://doi.org/10.1007/s13233-015-3099-9

Xu J, Liu X, Ren X, Gao G (2018) The role of chemical and physical crosslinking in different deformation stages of hybrid hydrogels. Eur Polym J 100:86–95. https://doi.org/10.1016/j.eurpolymj.2018.01.020

Xun X, Li Y, Zhu X, Zhang Q, Lu Y, Yang Z, Wan Y, Yao F, Deng X, Luo H (2021) Fabrication of robust, shape recoverable, macroporous bacterial cellulose scaffolds for cartilage tissue engineering. Macromol Biosci 21:2100167. https://doi.org/10.1002/mabi.202100167

Yin N, Stilwell MD, Santos TMA, Wang H, Weibel DB (2015) Agarose particle-templated porous bacterial cellulose and its application in cartilage growth in vitro. Acta Biomater 12:129–138. https://doi.org/10.1016/j.actbio.2014.10.019

Zaborowska M, Bodin A, Backdahl H, Popp J, Goldstein A, Gatenholm P (2010) Microporous bacterial cellulose as a potential scaffold for bone regeneration. Acta Biomater 6:2540–2547. https://doi.org/10.1016/j.actbio.2010.01.004

Zhan Z, Song Q, Zhou Z, Lu C (2019) Ultrastrong and conductive MXene/cellulose nanofiber films enhanced by hierarchical nano-architecture and interfacial interaction for flexible electromagnetic interference shielding. J Mater Chem C 7:9820–9829. https://doi.org/10.1039/C9TC03309B

Zhang H, Wang ZG, Zhang ZN, Wu J, Zhang J, He JS (2007) Regenerated-cellulose/multiwalled-carbon-nanotube composite fibers with enhanced mechanical properties prepared with the ionic liquid 1-Allyl-3-methylimidazolium chloride. Adv Mater 19:698–704. https://doi.org/10.1002/adma.200600442

Zhang W, Wang XC, Li XY, Zhang LL, Jiang F (2020) A 3D porous microsphere with multistage structure and component based on bacterial cellulose and collagen for bone tissue engineering. Carbohydr Polym 236:116043. https://doi.org/10.1016/j.carbpol.2020.116043

Zhang J, Ma Y, Han Y, Xu K, Yao S, Shi L, Zhu M (2023) 3D porous structure assembled from MXene via breath figure method for electrochemical detection of dopamine. Chem Eng J 452:139414. https://doi.org/10.1016/j.cej.2022.139414